ACS NANO

www.acsnano.org

ARTICLE

# Predicting Laser-Induced Colors of Random Plasmonic Metasurfaces and Optimizing Image Multiplexing Using Deep Learning

Hongfeng Ma, Nicolas Dalloz, Amaury Habrard, Marc Sebban, Florian Sterl, Harald Giessen, Mathieu Hebert, and Nathalie Destouches*

Cite This: *ACS Nano* 2022, 16, 9410−9419

Read Online

ACCESS | Metrics & More | Article Recommendations | Supporting Information

**ABSTRACT:** **Structural colors of plasmonic metasurfaces have been promised to a strong technological impact thanks to their high brightness, durability, and dichroic properties. However, fabricating metasurfaces whose spatial distribution must be customized at each implementation and over large areas is still a challenge. Since the demonstration of printed image multiplexing on quasi-random plasmonic metasurfaces, laser processing appears as a promising technology to reach the right level of accuracy and versatility. The main limit comes from the absence of physical models to predict the optical properties that can emerge from the laser processing of metasurfaces in which random metallic nanostructures are characterized by their statistical properties. Here, we demonstrate that deep neural networks trained from experimental data can predict the spectra and colors of laser-induced plasmonic metasurfaces in various observation modes. With thousands of experimental data, produced in a rapid and efficient way, the training accuracy is better than the perceptual just noticeable change. This accuracy enables the use of the predicted continuous color charts to find solutions for printing multiplexed images. Our deep learning approach is validated by an experimental demonstration of laser-induced two-image multiplexing. This approach greatly improves the performance of the laser-processing technology for both printing color images and finding optimized parameters for multiplexing. The article also provides a simple mining algorithm for implementing multiplexing with multiple observation modes and colors from any printing technology. This study can improve the optimization of laser processes for high-end applications in security, entertainment, or data storage.**

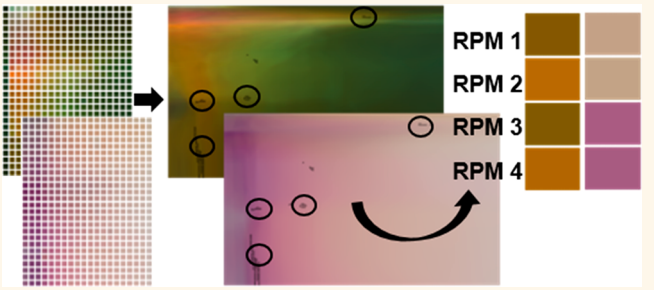


**KEYWORDS:** *plasmonics, deep learning, image multiplexing, random metasurface, laser-generated nanostructures*



Plasmonic colors, which result from a resonant interaction of light with metallic nanostructures, have strong assets for inventing innovative applications, which hold in a nanometer thick layer and are resistant to aging. Their ultimate spatial resolution allows considering their use for high-resolution digital cameras,[1] data storage,[2] or hyperspectral imaging.[3] Their sensitivity to light polarization, to the refractive index of their close environment, to the near- or far-field coupling between closely packed metal nanostructures, or to an electrical bias enables the fabrication of tunable color filters,[4−6] chemical sensors,[7,8] stretching detectors,[9] or active chameleon surfaces.[10] If plasmonic devices are often confined to micrometer sizes, some applications require nanostructuring metal−dielectric surfaces over large areas. It is precisely the case when visual effects are expected to be observed with the naked eye.

Recently, plasmonic random metasurfaces produced by laser over large areas have demonstrated peculiar metamerism enabling three-image multiplexing, where images are demultiplexed by the naked eye under natural light.[11,12] This approach greatly expands the scope of image multiplexing compared to techniques involving holographic images[13−18] or printed images[11,12,19−23] encoded with well-controlled plasmonic metasurfaces on small areas. Laser processing is easy to implement on large surfaces, cost-effective, rapid, and flexible,

Received: March 4, 2022
Accepted: May 31, 2022
Published: June 3, 2022

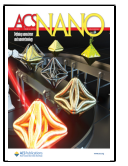

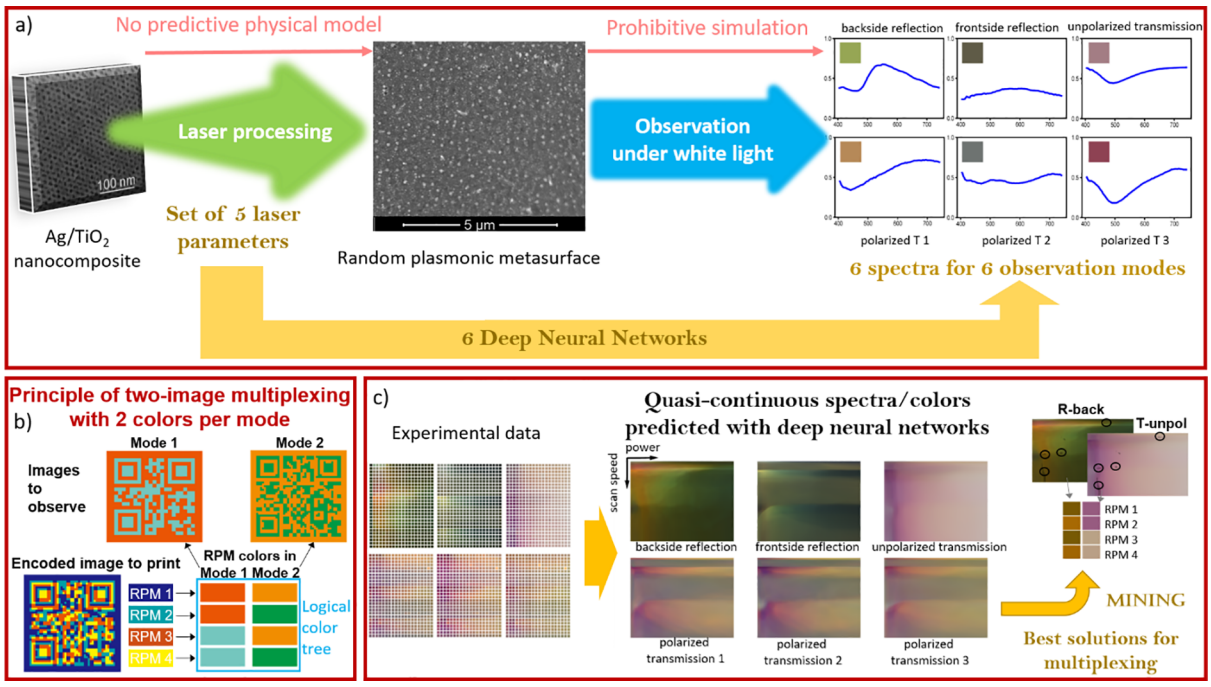


**Figure 1. (a) Rationale for the use of deep neural networks to predict the spectra and colors exhibited by a laser-processed random plasmonic metasurface (RPM) in various modes of observation. The measurement conditions in the six modes of observation are described in Methods. (b) Logical color tree fulfilled by a set of four RPMs, solution for two-image multiplexing, with bicolor images. The encoded image printed by laser contains the four RPMs. This encoded image gives rise to two different images (data matrices) when observed in modes 1 and 2. (c) Six deep neural networks are trained from experimental data to predict the spectra and colors observed in the six modes of observation (see Methods for details). A mining process among the simulated colors allows extracting all combinations of laser parameter sets that enable image multiplexing. With one laser parameter set leading to one random plasmonic metasurface, the solutions are given as sets of RPM.**

and it allows creating subwavelength gratings with a precise control of their orientation at the micrometer scale thanks to laser-induced self-organization mechanisms.[24−30] However, unlike usual metasurfaces, laser-induced random plasmonic metasurfaces are characterized by statistical parameters, due to the size inhomogeneity and spatial disorder, which are difficult to measure, and to predict. Indeed, no physical model presently links the laser-processing parameters to the statistical parameters of the laser-induced metasurfaces or to their optical properties. Predicting the colors, or spectra, exhibited by such metasurfaces in various observation modes over a large range of laser-processing parameters, and with a high accuracy where color gradients are steep, could greatly enhance the performance of laser-processing technologies.

Deep learning seems well-suited to tackle this multidimensional nonlinear problem. In this field of machine learning inspired by human brain, layered and hierarchical architectures of artificial neurons can be trained to interpolate nonlinear variations of multidimensional data from a huge amount of examples.[31−33] Deep learning led to breakthroughs in many fields such as speech recognition,[34] computer vision,[35] or particle physics.[36] During the recent past years, interest for coupling photonics and deep neural networks has grown tremendously with two main approaches: using waves controlled by photonic devices to accelerate computing speed of neural networks by analog calculation[37−39] or using deep learning to boost innovation and technological development in photonics.[40−48] Many efforts have been devoted to the design of nanostructures to get predefined far-field responses using deep neural networks with encoder and decoder-like models.[40,41] The inverse engineering can be achieved by neural networks provided that the loss function is differentiable.[44−47] But, most of the neural networks involved in photonic problems were trained from simulated data.

In this article, deep neural networks are used to predict the spectra, and colors, of laser-induced random plasmonic metasurfaces in different observation modes from the knowledge of laser-processing parameters. The neural networks are trained from experimental data, and special attention is paid to the loss function to get high accuracy in the prediction. The latter enables using the color charts predicted in the various observation modes for printed image multiplexing. A methodology is proposed to mine the laser-processing parameters space and find all the combinations that can be used to print multiplexed images. It unveils a lot of solutions that could not be found from the experimental database, which improves the optimization strategy. One of the best solutions is finally implemented experimentally, demonstrating that high-contrast images can be obtained in the two modes selected for multiplexing. The model proposes a general approach for implementing image multiplexing with various techniques and materials and can be expanded to other conditions of multiplexing.

## RESULTS AND DISCUSSION

**Laser-Induced Colors of Random Plasmonic Metasurfaces.** In this study, we use the same kind of laser-processed Ag NPs:$TiO_2$ metasurfaces as those used in our recent article demonstrating laser-induced three-printed image multiplexing.[12] 9,600 different random plasmonic metasurfaces (RPMs) are produced experimentally by varying five laser-


https://doi.org/10.1021/acsnano.2c02235
ACS Nano 2022, 16, 9410−9419

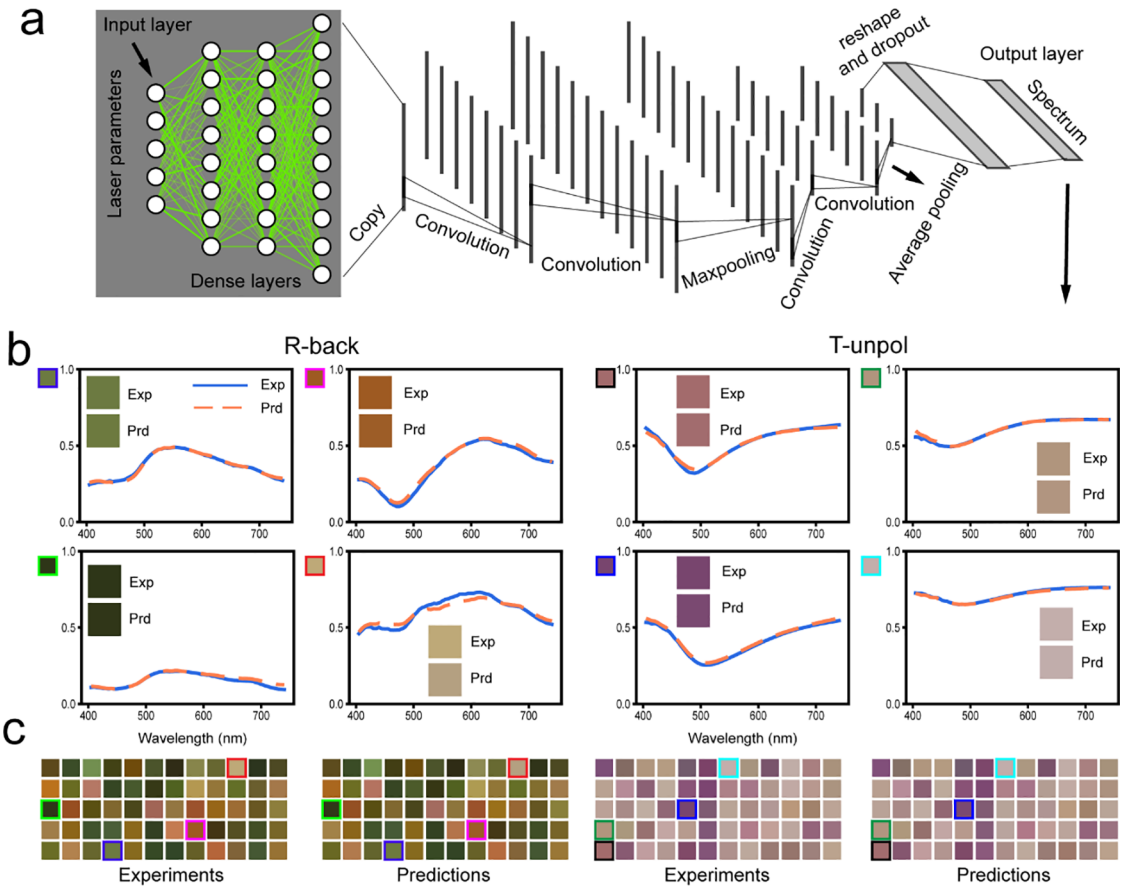


**Figure 2. (a) Architecture of the proposed neural network. (b) Comparison of predicted (Prd) and experimental (Exp) spectra showing various spectral errors. (c) Comparisons of sRGB colors calculated from experimental and predicted spectra. Squares with colored edges are the ones whose spectra are shown in panel b. All colors are calculated from the spectral data by using the CIE standard observer with a D65 illuminant.**

processing parameters whose values are given in Supporting Information Figure S1. The RPMs consist of a thin $TiO_2$ layer encapsulating Ag nanoparticles whose size distribution, anisotropy, and spatial distribution vary with the laser-processing parameters (scanning electron microscopy images of a selection of RPMs are shown in Supporting Information Figure S2 for illustration). The spectrum of each RPM is measured in six observation modes by a semiautomatic Fourier space microscopy setup[49] and normalized in each mode to take into account the eye adaptation to the maximum luminance in each mode (see Methods for details about the material, laser processing, and sample characterizations). After removal of faulty RPMs, six databases of 9,440 spectra and colors are obtained. Figure 1a illustrates the process used to create these databases, and highlights two limitations of the laser-processing technique to implement image multiplexing. First, no physical model allows predicting the statistical parameters that characterize the random plasmonic metasurfaces generated by laser processing. Second, the latter being complex and difficult to characterize, simulating the resulting colors is very demanding. We therefore introduce deep learning to accurately predict the colors induced by the laser parameters in different modes of observation. This color prediction intends not only to efficiently reproduce color images but also to unveil optimized solutions for printed image multiplexing. The latter requires one to find out particular RPMs whose colors form logical color trees such as the one shown in Figure 1b. In this article, six neural networks are trained to predict the colors in six modes of observation (Figure 1c). However, for the sake of clarity, only two modes are considered in the following; the full color measurements obtained on the four other modes are shown in Supporting Information Section S2 (Figures S3–S8). Backside reflection (R-back) and unpolarized transmission (T-unpol) modes are selected to demonstrate high-contrast image multiplexing for the naked eye observation under natural light.

**Neural Networks for Predicting Laser-Induced Spectra and Colors of Random Plasmonic Metasurfaces.** The architecture of the six feedforward neural networks (NNs) trained to predict the spectra in the six considered observation modes is the same (Figure 2a). These NNs take as input the five laser-processing parameters and give as output a 68-dimensional vector that stands for a spectrum. The first block consists of three successive dense layers, which feed a convolutional block that constructs the characteristics of the spectra. This block is composed of two consecutive sub-blocks each being made of two 1D convolution layers with ReLu activations followed by a pooling layer (maximum pooling and average pooling, respectively) block. The spectrum is finally obtained through a fully connected layer.

Beyond the architecture of the network, one key element of the model is the loss function minimized for optimizing the parameters. Our aim is to predict color with an accuracy better than the smallest color difference a human eye can perceive, also known as the perceptual just noticeable change. However,


https://doi.org/10.1021/acsnano.2c02235
ACS Nano 2022, 16, 9410−9419

**Table 1. Generalization Performance of the Optimized Neural Networks for Different Modes[a]**

| | $\Delta E_{76}$ | | $\Delta E_{94}$ | | $\Delta E_{00}$ | | spectral error, % | |
|---|---|---|---|---|---|---|---|---|
| loss (D65) | mean | SD | mean | SD | mean | SD | mean | SD |
| R-back | 1.99 | 2.08 | 1.38 | 1.45 | 1.38 | 1.45 | 1.18 | 1.39 |
| R-front | 1.02 | 0.88 | 0.89 | 0.78 | 0.86 | 0.70 | 0.94 | 1.01 |
| T-unpol | 0.80 | 0.82 | 0.66 | 0.69 | 0.67 | 0.63 | 0.71 | 0.93 |
| T-pol1 | 1.64 | 1.38 | 1.30 | 1.07 | 1.33 | 1.01 | 1.60 | 1.82 |
| T-pol2 | 1.92 | 1.76 | 1.51 | 1.38 | 1.51 | 1.28 | 1.77 | 2.20 |
| T-pol3 | 1.34 | 1.27 | 1.00 | 0.99 | 1.03 | 0.93 | 1.30 | 1.47 |
| Shi *et al.*[50] | | | | | 2.50 | 1.58 | | |

[a]The mean value and the standard deviation of each loss function are calculated over the test dataset in each mode. For the sake of comparison with ref 50, a loss function using the perceptual color difference $\Delta E_{00}$ is also calculated.

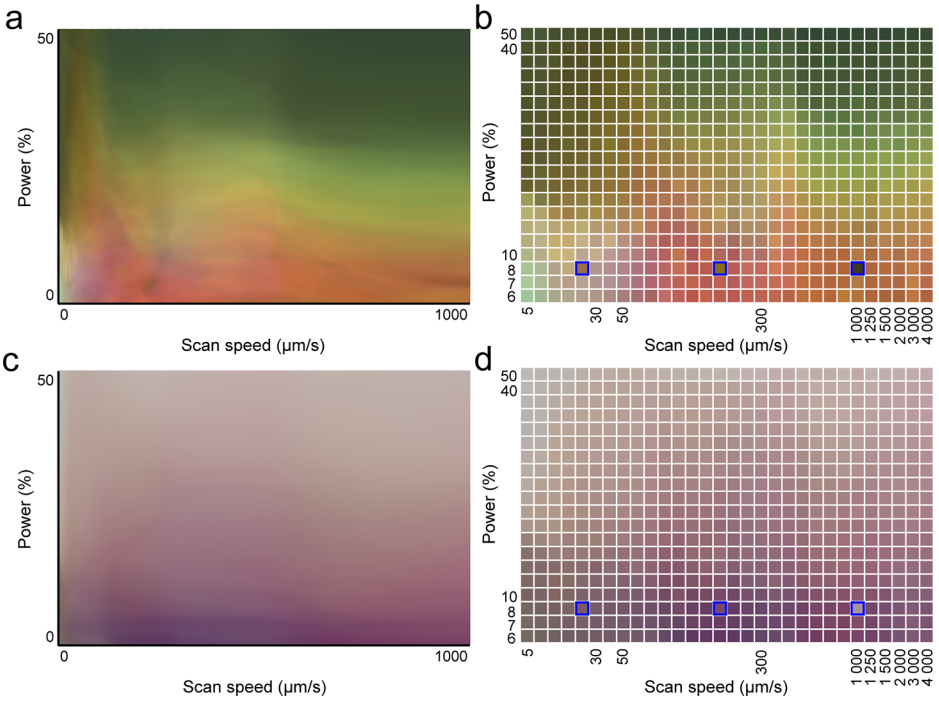


**Figure 3. Color charts of the neural network predictions for R-back (a) and T-unpol (c). Experimental data sets (ground truth) for R-back (b) and T-unpol (d). The repetition rate is fixed at 300 kHz, the linear laser polarization is horizontal, and the distance between successive laser scans is 2 $\mu$m. In the simulated color charts, the scan speed and power are uniformly sampled by 200 × 200 points ranging from 4 to 1,000 $\mu$m/s and from 5 to 50%, respectively. In the right column, pixels outlined in blue are outliers where the nanostructures are not well written and are not used for training or testing the neural network.**

when considering only the colorimetric distance between the predicted and experimental colors, the NN does not converge. In order to converge, but also to avoid overfitting, and to get a high accuracy in color prediction, the loss function is defined with three terms. These terms are fully described in Methods, which also explains why each of them is important to reach the results reported hereafter.

A total of 9,440 experimental data were available for training and testing each of the six neural networks, one for each mode. A set of 10% of the instances was kept for testing the model. The hyper-parameters of the network are tuned on the basis of a 6-fold cross-validation process to avoid trapping by local minima (Figure S9). The generalization capacity of our optimized network for the R-back and T-unpol modes is illustrated in Figure 2 and Table 1. The shape of the spectra is well-predicted on average, except in a very few cases as exemplified in the lower right example of the R-back mode (Figure 2b), and lead to a spectral loss $\epsilon_{spect}$ smaller than 1.77% in all modes. The color differences between the experimental and predicted data are good in average compared to the literature[50] (Table 1). This is also illustrated with sRGB colors in Figure 2c (more examples are reported in Figures S10–S15). Slight differences in the prediction accuracy are observed from one mode to another (Table 1) and are mainly related to the changes in the color gamut volume. A smaller gamut leads to a higher accuracy. Color gamuts in the CIE1976 L*a*b* color space are plotted in Figure S16. The interested reader can also look at the dispersion of the spectral loss within the six gamuts in Figure S17.

The trained neural networks not only reproduce the experimental colors but also interpolate continuous color changes with respect to laser parameters. In Figure 3, high-resolution charts of colors predicted in R-back and T-unpol modes are compared with the colors deduced from the measured experimental spectra, when varying scan speed and laser power. More colors are displayed in Figure S18 when varying the five laser-processing parameters. For the sake of comparison, Figure S19 and Table S1 show the low accuracy


https://doi.org/10.1021/acsnano.2c02235
ACS Nano 2022, 16, 9410−9419

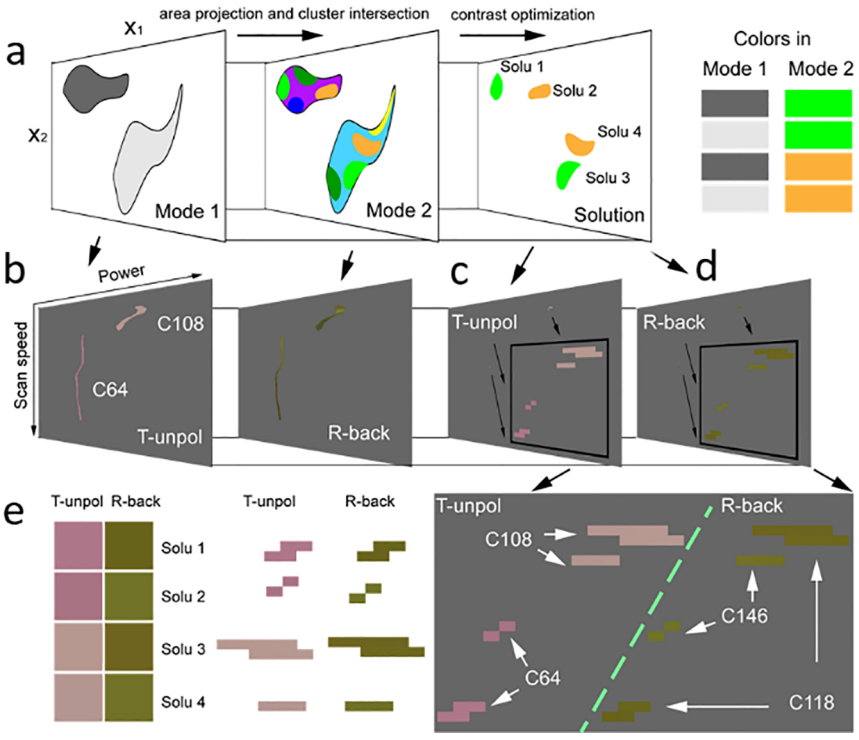


**Figure 4. Solutions for two-image multiplexing. (a) Principle of the algorithm designed to identify all of the subsets of RPMs that form a color tree. (b) Example of two true clusters selected in mode T-unpol whose contours are projected in mode R-back. (c and d) Results or the cluster intersection in the two modes. In this case, clusters C108 and C64 of mode T-unpol both intersect clusters C118 and C146 of mode R-back and form a solution for two-image multiplexing whose logical color tree is drawn in panel e with the shape of the subclusters that form the solutions. Each pixel corresponds to one particular RPM. When several solutions are found, only the ones exhibiting the highest color contrast in each mode are kept.**

on the predicted colors obtained by replacing the deep learning approach with an average over the four closest colors. The finely resolved color variations predicted by the trained neural networks are going to unveil all of the possible solutions for printed image multiplexing and allow the selection of the best one in terms of color contrast. The proposed methodology is presented in the next section.

**Color Mining and Multiplexing Algorithm.** Each set of laser parameters is now linked to a series of six different spectra through a bijective application, since none of the predicted combinations of six spectra is equal to another. Consequently, each laser parameter set must also correspond to a different RPM, and from now, we identify a RPM to a laser parameter set. The RPM sets that can be used to print multiplexed images must satisfy a logical color tree, such as the one shown in Figure 1c for two colors per mode and two images to display independently in two different modes. More complex color trees can be found in references.[11,12] A simple and compact algorithm is proposed to mine the simulated color sets and find out all of the solutions for two-image multiplexing with two colors per mode. The algorithm contains three main steps described hereafter.

*Clustering of Each Mode.* A hierarchical clustering with complete linkage is implemented in each mode for grouping colors. The criterion is the Euclidean distance $\Delta E_{76} < 2.2$ that corresponds to the colorimetric distance from which a color difference is noticeable. The use of $\Delta E_{76}$ was preferred compared to $\Delta E_{94}$ or $\Delta E_{00}$ because it strongly decreases the calculation time for clustering without deteriorating the results significantly. From this step, all the colors present in the same cluster are referred to by their cluster index. The 40,000 rpms of the predicted color charts (Figure 3a,c) give rise to 845 clusters in the R-back mode and to 173 clusters in the T-unpol modes. This difference is due to a larger color gamut in the R-back mode. One RPM belongs to one and only one cluster in one mode. Thus, there is no overlapping between clusters in one mode. The minimum number of RPMs in one cluster is one. The clusters are identified in the CIE 1976 L*a*b* color space and can appear as discontinuous areas in the color charts of Figure 3a,c, where RPM are ordered relative to the laser-processing parameters. For the sake of illustration, Figure 4b shows how two clusters in the T-unpol mode (C64 and C108) arrange in a selection (zoom) of the full predicted color chart.

*Cluster Intersections between Modes.* Once each predicted color chart is split into clusters, the algorithm starts searching the RPMs that form a logical tree. The geometrical approach implemented is illustrated in Figure 4a with a colored sketch, and in Figure 4b with the colors and clusters found in our samples. The mode with the lowest number of clusters (T-unpol) is chosen as the first mode to limit the calculation time. One pair of clusters is selected in this mode, and their contours are projected onto the color chart of the second mode. If at least two identical clusters of mode 2 are present within the contours of both clusters of mode 1, then the RPMs belonging to this cluster intersection are solutions for multiplexing. In Figure 4a, it is the case for the areas colored in light green, dark green, and orange in mode 2. One example of solution is reported in the third plot of Figure 4a. To find all of the possible solutions, one has to repeat this procedure for each pair of clusters of mode 1, requiring iteration for the $\frac{173(173-1)}{2} - 1$ other possible pairs of clusters of this mode.


https://doi.org/10.1021/acsnano.2c02235
ACS Nano 2022, 16, 9410−9419

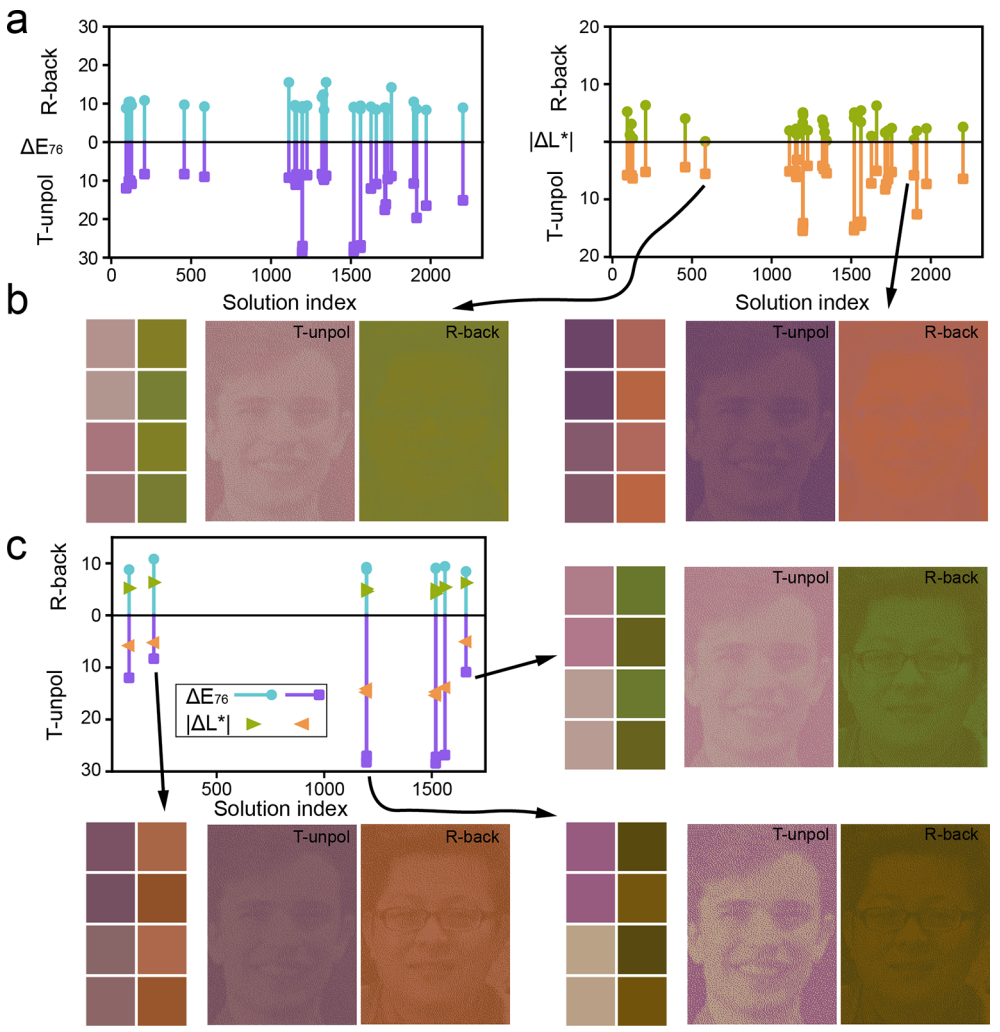


**Figure 5. Contrast optimization. (a) Color difference $\Delta E_{76}$ and perceptual lightness difference $|\Delta L^*|$ between the two colors in R-back mode and the two colors in T-unpol mode that form a solution for multiplexing. Only the 25 solutions that satisfy the following criterion, $\Delta E_{76} > 8.3$, in both modes, are displayed. (b) Simulated colors of the four RPMs that form the solutions of indices 583 and 1,894 and simulated images that should be observed in the T-unpol and R-back modes when using these solutions. Solution 583 exhibits $\Delta E_{76}$ and $|\Delta L^*|$ values of (9.0; 5.6) for T-unpol and (9.2; 0.1) for R-back modes. Solution 1,894 shows $\Delta E_{76}$ and $|\Delta L^*|$ values of (10.8; 5.8) for T-unpol and (10.5; 0.3) for R-back modes. (c) Best results after filtering with criteria $\Delta E_{76} > 8.3$ and $\Delta L > 4.2$. Solution 208 with $\Delta E_{76}$ and $|\Delta L^*|$ values of (8.3; 5.2) for T-unpol and (10.8; 6.3) for R-back modes. Solution 1,196 with $\Delta E_{76}$ and $|\Delta L^*|$ values of (28.2; 14.8) for T-unpol and (9.3; 5.1) for R-back modes. Solution 1,659 with $\Delta E_{76}$ and $|\Delta L^*|$ values of (10.9; 5.1) for T-unpol and (8.4; 6.3) for R-back modes. Photographs of authors N.Da. and H.M. are used in this figure.**

In Figure 4b, two true clusters of T-unpol mode, C64 and C108, are plotted and their contours projected in mode R-back, where they intersect the same clusters, C146 and C118, of mode 2. A zoom on these intersections is plotted in Figure 4c for mode 1 and in Figure 4d for mode 2 and is further enlarged just below in the chart of Figure 4e. The latter also illustrates the corresponding logical color tree with, for each solution named "solu", all of the RPMs that can be used to print the encoded multiplexed image.

*Contrast Maximization.* When more than two clusters in mode R-back are found to intersect the two clusters selected in the T-unpol mode, only the pair of clusters showing the highest color contrast in the mode R-back is kept. The color contrast in this study is defined as $\Delta E_{76} + |\Delta L^*|$, where $|\Delta L^*|$ stands for the absolute lightness difference. The importance of using $|\Delta L^*|$ is illustrated in the next section. After iterating the algorithm for all pairs of clusters of mode 1, a set of solutions is obtained, among which the best solutions can be selected using again the color contrast to filter the solutions.

The size of the subclusters that are solutions for multiplexing is always small, but it can contain several RPMs that can all be used as solutions for multiplexing. If the number of laser-processing parameter values is significantly reduced in the simulated color chart (undersampling), less solutions for multiplexing are found. This is especially what happens when the experimental data sets are used rather than the simulated data sets (see Figure S20). Color prediction by neural networks appears thus as a crucial step to identify the best combinations of laser-processing parameters.

**Implementation on the Full Data Set and Optimization.** The proposed algorithm is applied to a database of 160,000 rpms whose spectra are predicted in the R-back and T-unpol modes by using 200 different scan speeds, 200 powers, two laser repetition rates, and two distances between laser lines (sRGB colors plotted in Figure S18). The clustering



https://doi.org/10.1021/acsnano.2c02235
ACS Nano 2022, 16, 9410−9419

process on the whole data set costs 253 GB memory and 20 min. The number of clusters in the R-back mode is 2,810 and 508 in the T-unpol mode. By applying the two-mode and two colors per mode multiplexing algorithm, 2,239 solutions are found before the final color contrast filtering. Figure 5a shows the color difference $\Delta E_{76}$ and the perceptual lightness difference $|\Delta L^*|$ between the two colors found in R-back or in T-unpol mode for the solutions that satisfy the criterion $\Delta E_{76} > 8.3$. The last value was chosen arbitrarily in order to select less than 25 solutions. All of these solutions present a rather high color difference. However, when $|\Delta L^*| < 1$, the images are almost not perceptible, as illustrated in Figure 5b in the R-back mode. This result demonstrates that using only the color difference for optimizing the image is inadequate and must be completed by the perceptual lightness difference, to get highly contrasted images. Figure 5c shows the best solutions obtained when applying the criterion $\Delta E_{76} > 8.3$ and $|\Delta L^*| > 4.2$. The last value was adjusted to keep between 5 and 10 solutions. For the solutions displayed, the image contrast is now good enough to perceive the images in both modes.

**Robustness of the Solutions.** The proposed model based on neural networks, clustering, mining, and filtering algorithms is a general approach for implementing image multiplexing with a kind of printing technology. It can also be used for showing parameter ranges where there is a higher probability to find solutions for multiplexing. To understand the influences of the laser-processing parameters, all of the high-contrast solutions ($\Delta E_{76} > 8.3$ and $|\Delta L^*| > 4.2$) are plotted in parallel axes, as shown in Figure 6a. For all solutions, except index 208, the random nanostructures are induced under two different repetition rates (300 kHz and 600 kHz). Actually, it is observed that the two different repetition rates provide solutions with different perceptual lightness in T-unpol while maintaining a similar contrast in the R-back mode. The preferable distance between laser scans is 10 $\mu$m. When the laser power is around 10% and scan speed ranges from 700 to 1000 $\mu$m/s, the probability to find highly contrasted solutions is the highest. This can be useful to optimize the printing of experimental databases that will lead to high-contrast multiplexed images.

Finally the robustness of the predicted solutions is validated by using one of the best solutions found for two images and two colors per mode to print a proof of concept by laser. The gray scale pictures of the two first coauthors are first converted into binary images, with only black and white pixels, in which gradients are rendered thanks to an error diffusion algorithm. Then, these two binary images are combined to create an encoded image, which is printed by nanosecond laser with four RPMs made of Ag:$TiO_2$, selected to optimize the contrast $|\Delta L^*|$ rather than $\Delta E_{76}$ in each mode. The photographs of the experimental sample recorded in the R-back and T-unpol modes with nonpolarized white light are displayed in Figure 6b.

**Extension to Multiple Colors and Multiple Images.** The proposed multiplexing algorithm is compact and can be extended to multimodes (multi-images) and more than two colors per mode. To find solutions to three-image multiplexing, one has to start from a solution for two-image multiplexing. Once the four subclusters are selected in the first two modes. The projected areas of each subcluster in the third mode must intersect at least the same pair of clusters of the third mode. If more than two clusters of the third mode intersect each

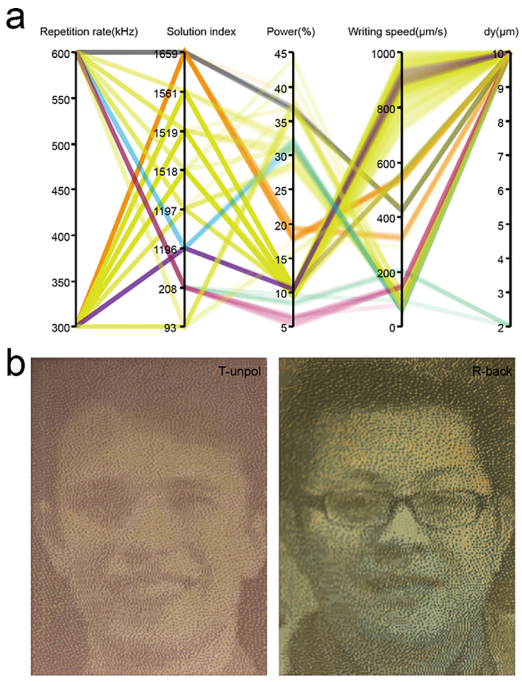


**Figure 6. Implementation of two-image multiplexing. (a) Multidimensional view of the high-contrast solutions for two-mode multiplexing deduced from predictions by neural networks and mining of the best solutions for multiplexing. (b) Two photographs of a physical sample produced with our laser-processing technique demonstrating the multiplexing of two images in the modes T-unpol and R-back. The multiplexed image is printed once on a single Ag:$TiO_2$ thin layer with only four different RPMs. Photographs of authors N.Da. and H.M. are used in this figure.**

subcluster of the solution for two-image multiplexing, then a contrast-based selection is applied. The intersections make appear eight subclusters that are solutions for three-image multiplexing (illustrated in Figure S21). A set of $2^3$ RMPs form a solution for three-image multiplexing. It is clear that this process can be stacked and extended to $N$-image multiplexing iteratively and the number of different nanostructures needed is $2^N$.

The proposed algorithm is also easily extendable for multicolor multiplexing (illustrated in Figure S22). Finally, the algorithm in its shape is easily extendable to $M$-colors and $N$-modes, which requires $M^N$-kinds of RPMs. The limit is to have RPMs and modes that can satisfy such conditions.

## CONCLUSIONS

We propose a four-step approach using deep learning to predict the laser-induced colors of random plasmonic metasurfaces in different modes of observation and print highly contrasted multiplexed images. The neural networks are trained, validated, and tested over 9,440 laser-processed samples whose spectra are measured in six different observation modes by a semiautomatic Fourier space microscopy setup. The peculiarity of the deep learning model comes from the hybrid nature of the loss function used to optimize the inner parameters of the network, which takes into account both the shape of the predicted spectra and the capacity to generate colors that are perceptually relevant. The high accuracy of the predicted colors enables their use for finding all of the possible solutions to image multiplexing offered by the technology and to select the ones leading to


https://doi.org/10.1021/acsnano.2c02235
ACS Nano 2022, 16, 9410−9419

highly contrasted images. The performance of the approach is demonstrated by implementing image multiplexing on a physical sample. The simplicity of the observation conditions, with the naked eye and under nonpolarized white light, the absence of cross-talk between images, and the simplicity of fabrication with direct nanosecond laser writing make the technology very promising for industrial applications.

The introduction of deep learning in the process considerably increases the performance of laser processing to print colored and multiplexed images on plasmonic metasurfaces as it unveils optimized solutions for multiplexing that could not be found from roughly sampled experimental data. The mining process, extendable to *M*-color *N*-image multiplexing, is a paradigm for selecting colors of random nanostructures in different modes of observation for multiplexing and can find various applications in other fields such as entertainment, data storage, or security.

## METHODS

**Experiments.** *Initial Sample Preparation.* Following a protocol fully described in ref 11, 200 ±30 nm thick mesoporous $TiO_2$ thin films are elaborated by sol−gel process on glass slides . The films are soaked in a silver nitrate solution (0.85 M) and exposed to UV light (254 nm, 6 mW/cm$^2$) for 5 min to fill the pores with Ag ions, Ag atoms, and small Ag nanoparticles, as described in ref 51.

*Laser Processing.* A nanosecond (1.3 ns pulse duration) fiber laser (IPG Photonics) emitting at 532 nm wavelength scans the sample surface by means of a scanner head equipped with a 16 cm F-Theta lens, giving a laser spot diameter at $1/e^2$ of 13.5 $\mu$m and a maximum fluence of 8.5 J/cm$^2$ at 600 kHz. The laser fluence is deduced from the laser power given in the article as follows:

$$\text{fluence (J/cm}^2) = \frac{\text{power (W)}}{\text{effective area (cm}^2) \times \text{repetition rate(Hz)}}$$

The laser is linearly polarized using a Brewster-angle polarizer, and the polarization can be rotated by a half-wave plate. The 9,600 metasurfaces are created over 72 mm$^2$ square pixels, which are drawn by hatching each square with laser lines, separated by an interline distance named dy, parallel to the diagonal at a constant scan speed, laser power, repetition rate, and polarization orientation. To build the initial database, 9,600 sets of these laser-processing parameters were chosen; their values are given in Figure S1. The layer thickness of the Ag NPs:$TiO_2$ films varies with the laser-processing parameters typically between 80 and 150 nm.

*Measurement and Normalization of Spectra.* Spectral characterization measurements are performed with a microspectroscopy setup based on a Nikon TE2000-U inverted microscope in combination with an imaging spectrometer consisting of a Princeton Instruments SP2500i grating monochromator and a PIXIS-256 Peltier-cooled CCD camera. The sample is mounted in a motorized stage (Märzhäuser) in the microscope sample plane. The microscope is connected to the spectrometer *via* a modified 4-f relay, which projects the Fourier plane instead of the image plane onto the spectrometer entrance slit.[49] In this way, an angle-resolved image can be recorded. An iris in the microscope image plane is used to only select light from a single field on the sample at a time.

To measure spectral reflectances, the sample is illuminated by a fiber-coupled halogen lamp *via* a Köhler illumination setup through the objective (100×, NA 0.9). The measured signal is normalized using an Au mirror. The accessible-angle range is limited by the objective NA. For spectral transmittance measurements, a critical illumination path is used to illuminate the sample *via* a condenser with the same light source. In this case, the condenser lens NA (0.65) is limiting. Polarizers are inserted above the condenser lens and below the microscope objective. A custom-built LabView-based software package is used to automatically record the spectral transmittance and reflectance.

Measurements in reflection are carried out with nonpolarized light and averaged over the incidence-angle range [13°; 17°] when the sample is illuminated from the film side (frontside reflection) or from the substrate side (backside reflection). Measurements in transmission mode are carried out under normal incidence with nonpolarized light (unpolarized transmission) or when placing the sample between two polarizers with three different angular configurations. Polarized transmission 1 corresponds to the configuration where the polarizer axis is parallel to the 0° laser polarization and the analyzer axis is at 80° from the polarizer axis. In polarized transmission 2, the two polarizers are rotated by 60° compared with polarized transmission 1. In polarized transmission 3, the two polarizers are rotated by 120° compared with polarized transmission 1.

A custom-built LabView-based software package is used to automatically record the spectral transmittance and reflectance for all positions on the sample by moving the XY stage. All measured spectra are further filtered with a moving average resulting in a 5 nm spectral resolution.

The final step is a normalization of all spectra based on colorimetric considerations to take into account eye adaptation to the maximum luminance in each observation mode. The proposed procedure is explained in Section S2. The spectra used for training the neural networks are those obtained after this last normalization step.

**Neural Networks.** The loss function is made of two terms, a spectrum loss, $\epsilon_{\text{spect}}$, and a perceptual color loss including $\epsilon_{\Delta E_{94}}$ and $\epsilon_{\Delta E_{76}}$ defined as follows:

$$\epsilon_{\text{spect}} = \frac{\sum_i^N |\varphi_i - \varphi_i^*|}{N} \tag{1}$$

where $\varphi_i$ is the $i$th training spectrum, $N$ is the batch size, and $\varphi_i^*$ is the predicted spectrum. Note that a mean absolute deviation is used rather than a standard least-squares error to prevent the algorithm from overfitting outliers. The two terms of the perceptual color loss are defined as

$$\epsilon_{\Delta E_{94}} = \frac{\sum_i^N \Delta E_{94}(\varphi_i, \varphi_i^*)}{N} \tag{2}$$

$$\epsilon_{\Delta E_{76}} = \frac{\sum_i^N \Delta E_{76}(\varphi_i, \varphi_i^*)}{N} \tag{3}$$

where $\Delta E_{94}(\varphi_i,\varphi_i^*)$ and $\Delta E_{76}(\varphi_i,\varphi_i^*)$ are the perceptual color differences, in the definitions of 1994 and 1976, respectively, between the predicted and training spectra. The global loss function is defined as the following linear combination:

$$\epsilon = \begin{cases} \epsilon_{\text{spect}}, & \text{if } \epsilon_{\Delta E_{94}} > 10 \\ \epsilon_{\text{spect}} + \alpha\epsilon_{\Delta E_{94}} + \beta\epsilon_{\Delta E_{76}}, & \text{otherwise} \end{cases} \tag{4}$$

In this work, the scaling factors are set to $\alpha = 0.1$ and $\beta = 1.0$, which have been shown to be robust for all the modes. The $\Delta E_{94}$ perceptual color difference is more relevant than $\Delta E_{76}$ to discriminate colors that are close to each other. However, it appears to be not reliable anymore to measure colorimetric distances when its value is large (typically larger than 10), leading to divergence if it is used from the beginning. The combination of the two perceptual color losses appears to improve the results accuracy, compared to the use of $\epsilon_{\Delta E_{76}}$ only, and the reliability of the trained network in the different modes.

The neural networks are optimized using several techniques such as cross-validation, dropout, and regularization. Each data set consists of 9,440 samples. All works are performed on the basis of PyTorch,[52] ver. 1.5, with graphic card GTX1080Ti on clusters with an Ubuntu system at Laboratoire Hubert Curien. For each mode, the optimization process costs 2 weeks before finishing.



https://doi.org/10.1021/acsnano.2c02235
ACS Nano 2022, 16, 9410−9419

## CLUSTERING

The grouping of colors is performed using agglomerative clustering or hierarchical clustering with complete linkage, known as unsupervised learning methods. While the K-means method is commonly used in clustering, we noticed that the hierarchical clustering with complete linkage was more robust in giving the same clustering tree on running at different times. The clustering is conducted using Python with scikit-learn,[53] ver. 0.24.0. For 160,000 CIELAB data, the program takes over 250 GB memory in an Ubuntu system with Intel Xeon Gold 6136.

## ASSOCIATED CONTENT

### Supporting Information

The Supporting Information is available free of charge at https://pubs.acs.org/doi/10.1021/acsnano.2c02235.

Laser-processing parameters and laser-induced RPMs; data set preparation; hyper-parameter tuning; solutions for two-image multiplexing; extended multiplexing algorithm (PDF)

## AUTHOR INFORMATION


### Corresponding Author

**Nathalie Destouches** − *Laboratoire Hubert Curien, CNRS UMR 5516, Institut d'Optique Graduate School, 42000 St-Etienne, France;* orcid.org/0000-0002-3843-6382; Email: nathalie.destouches@univ-st-etienne.fr

### Authors

**Hongfeng Ma** − *Laboratoire Hubert Curien, CNRS UMR 5516, Institut d'Optique Graduate School, 42000 St-Etienne, France;* orcid.org/0000-0003-3160-3990

**Nicolas Dalloz** − *Laboratoire Hubert Curien, CNRS UMR 5516, Institut d'Optique Graduate School, 42000 St-Etienne, France; HID Global CID SAS, 92150 Suresnes, France*

**Amaury Habrard** − *Laboratoire Hubert Curien, CNRS UMR 5516, Institut d'Optique Graduate School, 42000 St-Etienne, France*

**Marc Sebban** − *Laboratoire Hubert Curien, CNRS UMR 5516, Institut d'Optique Graduate School, 42000 St-Etienne, France*

**Florian Sterl** − *4th Physics Institute and Research Center SCoPE, University of Stuttgart, 70569 Stuttgart, Germany;* orcid.org/0000-0002-1025-6777

**Harald Giessen** − *4th Physics Institute and Research Center SCoPE, University of Stuttgart, 70569 Stuttgart, Germany*

**Mathieu Hebert** − *Laboratoire Hubert Curien, CNRS UMR 5516, Institut d'Optique Graduate School, 42000 St-Etienne, France*

Complete contact information is available at: https://pubs.acs.org/10.1021/acsnano.2c02235


### Notes

The authors declare no competing financial interest.

## ACKNOWLEDGMENTS

We acknowledge Francis Vocanson for providing the Ag:$TiO_2$ thin films on which the experiments have been carried out and Balint Eles for assistance with the scanning electron microscopy analysis in the Supporting Information. H.M., N.Da., M.H., and N.De. acknowledge the ANR for funding through Project MIXUP (ANR-18-CE39-0010). N.Da. is employed by the company HID Global CID.

## REFERENCES


(1) Yokogawa, S.; Burgos, S. P.; Atwater, H. A. Plasmonic Color Filters for CMOS Image Sensor Applications. *Nano Lett.* **2012**, *12*, 4349−4354.

(2) Kumar, K.; Duan, H.; Hegde, R. S.; Koh, S. C. W.; Wei, J. N.; Yang, J. K. W. Printing Colour at the Optical Diffraction Limit. *Nat. Nanotechnol.* **2012**, *7*, 557−561.

(3) Stewart, J. W.; Vella, J. H.; Li, W.; Fan, S.; Mikkelsen, M. H. Ultrafast Pyroelectric Photodetection with On-Chip Spectral Filters. *Nat. Mater.* **2020**, *19*, 158−162.

(4) Franklin, D.; Frank, R.; Wu, S.-T.; Chanda, D. Actively Addressed Single Pixel Full-Colour Plasmonic Display. *Nat. Commun.* **2017**, *8*, 15209.

(5) Xiong, K.; Tordera, D.; Emilsson, G.; Olsson, O.; Linderhed, U.; Jonsson, M. P.; Dahlin, A. B. Switchable Plasmonic Metasurfaces with High Chromaticity Containing Only Abundant Metals. *Nano Lett.* **2017**, *17*, 7033−7039.

(6) Xu, T.; Walter, E. C.; Agrawal, A.; Bohn, C.; Velmurugan, J.; Zhu, W.; Lezec, H. J.; Talin, A. A. High-Contrast and Fast Electrochromic Switching Enabled by Plasmonics. *Nat. Commun.* **2016**, *7*, 10479.

(7) Duan, X.; Kamin, S.; Liu, N. Dynamic Plasmonic Colour Display. *Nat. Commun.* **2017**, *8*, 14606.

(8) Chen, Y.; Duan, X.; Matuschek, M.; Zhou, Y.; Neubrech, F.; Duan, H.; Liu, N. Dynamic Color Displays Using Stepwise Cavity Resonators. *Nano Lett.* **2017**, *17*, 5555−5560.

(9) Tseng, M. L.; Yang, J.; Semmlinger, M.; Zhang, C.; Nordlander, P.; Halas, N. J. Two-Dimensional Active Tuning of an Aluminum Plasmonic Array for Full-Spectrum Response. *Nano Lett.* **2017**, *17*, 6034−6039.

(10) Wang, G.; Chen, X.; Liu, S.; Wong, C.; Chu, S. Mechanical Chameleon through Dynamic Real-Time Plasmonic Tuning. *ACS Nano* **2016**, *10*, 1788−1794.

(11) Destouches, N.; Sharma, N.; Vangheluwe, M.; Dalloz, N.; Vocanson, F.; Bugnet, M.; Hébert, M.; Siegel, J. Laser-Empowered Metasurfaces for White Light Image Multiplexing. *Adv. Funct. Mater.* **2021**, *31*, 2010430.

(12) Dalloz, N.; Le, V. D.; Hebert, M.; Eles, B.; Flores Figueroa, M. A.; Hubert, C.; Ma, H.; Sharma, N.; Vocanson, F.; Ayala, S.; et al. Anti-Counterfeiting White Light Printed Image Multiplexing By Fast Nanosecond Laser Processing. *Adv. Mater.* **2022**, *34*, 2104054.

(13) Arbabi, A.; Horie, Y.; Bagheri, M.; Faraon, A. Dielectric Metasurfaces for Complete Control of Phase and Polarization with Subwavelength Spatial Resolution and High Transmission. *Nat. Nanotechnol.* **2015**, *10*, 937−943.

(14) Deng, L.; Deng, J.; Guan, Z.; Tao, J.; Chen, Y.; Yang, Y.; Zhang, D.; Tang, J.; Li, Z.; Li, Z.; Yu, S.; Zheng, G.; Xu, H.; Qiu, C.-W.; Zhang, S. Malus-Metasurface-Assisted Polarization Multiplexing. *Light-Sci. Appl.* **2020**, *9*, 101.

(15) Zhao, R.; Sain, B.; Wei, Q.; Tang, C.; Li, X.; Weiss, T.; Huang, L.; Wang, Y.; Zentgraf, T. Multichannel Vectorial Holographic Display and Encryption. *Light-Sci. Appl.* **2018**, *7*, 95.

(16) Deng, J.; Deng, L.; Guan, Z.; Tao, J.; Li, G.; Li, Z.; Li, Z.; Yu, S.; Zheng, G. Multiplexed Anticounterfeiting Meta-Image Displays with Single-Sized Nanostructures. *Nano Lett.* **2020**, *20*, 1830−1838.

(17) Lim, K. T. P.; Liu, H.; Liu, Y.; Yang, J. K. W. Holographic Colour Prints for Enhanced Optical Security by Combined Phase and Amplitude Control. *Nat. Commun.* **2019**, *10*, 25.

(18) Wen, D.; Cadusch, J.; Meng, J.; Crozier, K. Multifunctional Dielectric Metasurfaces Consisting of Color Holograms Encoded into Color Printed Images. *Adv. Funct. Mater.* **2020**, *30*, 1906415.

(19) Goh, X. M.; Zheng, Y.; Tan, S. J.; Zhang, L.; Kumar, K.; Qiu, C.-W.; Yang, J. K. W. Three-Dimensional Plasmonic Stereoscopic Prints in Full Colour. *Nat. Commun.* **2014**, *5*, 5361.

(20) Bao, Y.; Yu, Y.; Xu, H.; Lin, Q.; Wang, Y.; Li, J.; Zhou, Z.-K.; Wang, X.-H. Coherent Pixel Design of Metasurfaces for Multidimen-

sional Optical Control of Multiple Printing-Image Switching and Encoding. *Adv. Funct. Mater.* **2018**, *28*, 1805306.
(21) Liu, H.; Xu, J.; Wang, H.; Liu, Y.; Ruan, Q.; Wu, Y.; Liu, X.; Yang, J. K. W. Tunable Resonator-Upconverted Emission (TRUE) Color Printing and Applications in Optical Security. *Adv. Mater.* **2019**, *31*, 1807900.
(22) Heydari, E.; Sperling, J. R.; Neale, S. L.; Clark, A. W. Plasmonic Color Filters as Dual-State Nanopixels for High-Density Microimage Encoding. *Adv. Funct. Mater.* **2017**, *27*, 1701866.
(23) Jang, J.; Jeong, H.; Hu, G.; Qiu, C.-W.; Nam, K. T.; Rho, J. Kerker-Conditioned Dynamic Cryptographic Nanoprints. *Adv. Opt. Mater.* **2019**, *7*, 1801070.
(24) Sharma, N.; Vangheluwe, M.; Vocanson, F.; Cazier, A.; Bugnet, M.; Reynaud, S.; Vermeulin, A.; Destouches, N. Laser-Driven Plasmonic Gratings for Hiding Multiple Images. *Mater. Horiz.* **2019**, *6*, 978−983.
(25) Sharma, N.; Destouches, N.; Florian, C.; Serna, R.; Siegel, J. Tailoring Metal-Dielectric Nanocomposite Materials with Ultrashort Laser Pulses for Dichroic Color Control. *Nanoscale* **2019**, *11*, 18779−18789.
(26) Liu, Z.; Siegel, J.; Garcia-Lechuga, M.; Epicier, T.; Lefkir, Y.; Reynaud, S.; Bugnet, M.; Vocanson, F.; Solis, J.; Vitrant, G.; Destouches, N. Three-Dimensional Self-Organization in Nanocomposite Layered Systems by Ultrafast Laser Pulses. *ACS Nano* **2017**, *11*, 5031−5040.
(27) Nyga, P.; Chowdhury, S. N.; Kudyshev, Z.; Thoreson, M. D.; Kildishev, A. V.; Shalaev, V. M.; Boltasseva, A. Laser-Induced Color Printing on Semicontinuous Silver Films: Red, Green and Blue. *Opt. Mater. Express* **2019**, *9*, 1528−1538.
(28) Roberts, A. S.; Novikov, S. M.; Yang, Y.; Chen, Y.; Boroviks, S.; Beermann, J.; Mortensen, N. A.; Bozhevolnyi, S. I. Laser Writing of Bright Colors on Near-Percolation Plasmonic Reflector Arrays. *ACS Nano* **2019**, *13*, 71−77.
(29) Zhu, X.; Vannahme, C.; Højlund-Nielsen, E.; Mortensen, N. A.; Kristensen, A. Plasmonic Colour Laser Printing. *Nat. Nanotechnol.* **2016**, *11*, 325−329.
(30) Zhu, X.; Yan, W.; Levy, U.; Mortensen, N. A.; Kristensen, A. Resonant Laser Printing of Structural Colors on High-Index Dielectric Metasurfaces. *Sci. Adv.* **2017**, *3*, No. e1602487.
(31) LeCun, Y.; Bengio, Y.; Hinton, G. Deep Learning. *Nature* **2015**, *521*, 436−444.
(32) Bishop, C. M. *Pattern Recognition and Machine Learning*; Springer-Verlag: New York, 2006.
(33) Goodfellow, I.; Bengio, Y.; Courville, A. *Deep Learning*; Adaptive Computation and Machine Learning Series; MIT Press: Cambridge, MA, USA, 2016.
(34) Hinton, G.; Deng, L.; Yu, D.; Dahl, G.; Mohamed, A.; Jaitly, N.; Senior, A.; Vanhoucke, V.; Nguyen, P.; Sainath, T.; Kingsbury, B. Deep Neural Networks for Acoustic Modeling in Speech Recognition: The Shared Views of Four Research Groups. *IEEE Signal Process. Mag.* **2012**, *29*, 82−97.
(35) Taigman, Y.; Yang, M.; Ranzato, M.; Wolf, L. DeepFace: Closing the Gap to Human-Level Performance in Face Verification. In *2014 IEEE Conference on Computer Vision and Pattern Recognition*, June 23−28, 2014, Columbus, OH, USA; IEEE, 2014; pp 1701−1708. DOI: 10.1109/CVPR.2014.220.
(36) Baldi, P.; Sadowski, P.; Whiteson, D. Searching for Exotic Particles in High-Energy Physics with Deep Learning. *Nat. Commun.* **2014**, *5*, 4308.
(37) Xu, X.; Tan, M.; Corcoran, B.; Wu, J.; Boes, A.; Nguyen, T. G.; Chu, S. T.; Little, B. E.; Hicks, D. G.; Morandotti, R.; Mitchell, A.; Moss, D. J. 11 TOPS Photonic Convolutional Accelerator for Optical Neural Networks. *Nature* **2021**, *589*, 44−51.
(38) Lin, X.; Rivenson, Y.; Yardimci, N. T.; Veli, M.; Luo, Y.; Jarrahi, M.; Ozcan, A. All-Optical Machine Learning Using Diffractive Deep Neural Networks. *Science* **2018**, *361*, 1004−1008.
(39) Mohammadi Estakhri, N.; Edwards, B.; Engheta, N. Inverse-Designed Metastructures That Solve Equations. *Science* **2019**, *363*, 1333−1338.
(40) Malkiel, I.; Mrejen, M.; Nagler, A.; Arieli, U.; Wolf, L.; Suchowski, H. Plasmonic Nanostructure Design and Characterization via Deep Learning. *Light-Sci. Appl.* **2018**, *7*, 60.
(41) Liu, D.; Tan, Y.; Khoram, E.; Yu, Z. Training Deep Neural Networks for the Inverse Design of Nanophotonic Structures. *ACS Photonics* **2018**, *5*, 1365−1369.
(42) Wiecha, P. R.; Muskens, O. L. Deep Learning Meets Nanophotonics: A Generalized Accurate Predictor for Near Fields and Far Fields of Arbitrary 3D Nanostructures. *Nano Lett.* **2020**, *20*, 329−338.
(43) Shi, L.; Li, B.; Kim, C.; Kellnhofer, P.; Matusik, W. Towards Real-Time Photorealistic 3D Holography with Deep Neural Networks. *Nature* **2021**, *591*, 234−239.
(44) Hughes, T. W.; Minkov, M.; Williamson, I. A. D.; Fan, S. Adjoint Method and Inverse Design for Nonlinear Nanophotonic Devices. *ACS Photonics* **2018**, *5*, 4781−4787.
(45) Mansouree, M.; McClung, A.; Samudrala, S.; Arbabi, A. Large-Scale Parametrized Metasurface Design Using Adjoint Optimization. *ACS Photonics* **2021**, *8*, 455−463.
(46) Wang, K.; Ren, X.; Chang, W.; Lu, L.; Liu, D.; Zhang, M. Inverse Design of Digital Nanophotonic Devices Using the Adjoint Method. *Photon. Res.* **2020**, *8*, 528−533.
(47) Jiang, J.; Fan, J. A. Global Optimization of Dielectric Metasurfaces Using a Physics-Driven Neural Network. *Nano Lett.* **2019**, *19*, 5366−5372.
(48) Zhou, J.; Huang, B.; Yan, Z.; Bünzli, J.-C. G. Emerging Role of Machine Learning in Light-Matter Interaction. *Light-Sci. Appl.* **2019**, *8*, 84.
(49) Sterl, F.; Strohfeldt, N.; Both, S.; Herkert, E.; Weiss, T.; Giessen, H. Design Principles for Sensitivity Optimization in Plasmonic Hydrogen Sensors. *ACS Sens.* **2020**, *5*, 917−927.
(50) Shi, L.; Babaei, V.; Kim, C.; Foshey, M.; Hu, Y.; Sitthi-Amorn, P.; Rusinkiewicz, S.; Matusik, W. Deep Multispectral Painting Reproduction via Multi-Layer, Custom-Ink Printing. *ACM Trans. Graph.* **2018**, *37*, 1−15.
(51) Liu, Z.; Vitrant, G.; Lefkir, Y.; Bakhti, S.; Destouches, N. Laser Induced Mechanisms Controlling the Size Distribution of Metallic Nanoparticles. *Phys. Chem. Chem. Phys.* **2016**, *18*, 24600−24609.
(52) Paszke, A.; Gross, S.; Massa, F.; Lerer, A.; Bradbury, J.; Chanan, G.; Killeen, T.; Lin, Z.; Gimelshein, N.; Antiga, L.; Desmaison, A.; Köpf, A.; Yang, E.; DeVito, Z.; Raison, M.; Tejani, A.; Chilamkurthy, S.; Steiner, B.; Fang, L.; Bai, J.; Chintala, S. PyTorch: An Imperative Style, High-Performance Deep Learning Library. In *NIPS 2019, Proceedings of the 33rd Conference on Neural Information Processing Systems*, Vancouver, BC, Canada, Dec. 8−14, 2019; Wallach, H., Larochelle, H., Beygelzimer, A., d'Alché-Buc, F., Fox, E., Garnett, R., Eds.; Neural Information Processing Systems Foundation (NIPS): Vancouver, BC, Canada, 2020; p 8026.
(53) Pedregosa, F.; Varoquaux, G.; Gramfort, A.; Michel, V.; Thirion, B.; Grisel, O.; Blondel, M.; Prettenhofer, P.; Weiss, R.; Dubourg, V.; Vanderplas, J.; Passos, A.; Cournapeau, D.; Brucher, M.; Perrot, M.; Duchesnay, E. Scikit-Learn: Machine Learning in Python. *J. Machine Learning Res.* **2011**, *12*, 2825−2830.